An Ultra Low-dimensional Inversion of Homogeneous Geobodies in Full Waveform Inversion

Ashutosh Tewari, Dimitar Trenev*
ExxonMobil Research & Engineering Company

Summary

We address the problem of inversion of large, nearly-homogeneous geobodies in a Full Waveform Inversion (FWI) framework. Of particular interest are subsurface salt bodies, as they are known to serve as seals for hydrocarbon reservoirs. Salt bodies offer a sharp contrast of material properties (with respect to their surroundings) to the incident seismic waves, which significantly reduces the transmission of signal through them. Thus, the presence of salt with unknown geometry presents formidable challenges to FWI as a subsurface imaging technique. To this end, we propose a low-dimensional representation of the salt bodies that is grounded on a stochastic view of the subsurface and treats the presence of salt as a spatial random process. In this setting, a salt body can be represented as a linear combination of a set of ordered, orthonormal basis functions with increasingly small marginal utility. Low-dimensionality is then achieved by truncating the number of basis functions to be included in this representation. The truncation can drastically reduce the dimension of the inversion space. When coupled with state-of-the-art optimization algorithms to minimize a loss function of FWI, the proposed representation is shown to recover the complete geometry of salt body, where traditional cell-based representation could only recover the top of it. Additionally, although the proof of concept pertains to the inversion of salt bodies, the methodology applies to any other nearly homogeneous geobody of interest.

Introduction

Seismic Full Wave-form Inversion (FWI) offers an attractive alternative to traditional imaging techniques, but results in a severely ill-posed inverse problem. Therefore, FWI -along with the fact that forward wave propagation models are costly- presents a formidable challenge to optimization algorithms. These challenges are exacerbated in the presence of salt bodies which create a highly reflective interface with its surroundings, thereby obscuring the subsalt reflectors. For this reason, traditional cell-based FWI often fails to image underneath the salt bodies. Salt inversion has received considerable attention by the oil & gas exploration community as salt bodies provide excellent seals for hydrocarbon reservoirs. A number of approaches have been proposed in this regard, ranging from post processing methods that try to delineate salt bodies (Moser, 2007; O'Briain, 2013; Maranganti, 2014) to more automated methods that try to directly invert for salt geometry (Lewis, 2012, Guo, 2013; Kadu, 2016; Kalita, 2018).

Our method falls in the category of shape-based inversion methods, wherein the inversion domain (Ω) naturally splits into a region Ω_s ($\subseteq \Omega$) representing a homogeneous body with unknown shape, separated from the background ($\Omega_{bg} = \Omega \backslash \Omega_s$) via the boundary $\partial\Omega_s$. Any spatially varying material property, m at location $x \in \Omega$, can then be represented as

$$m(x) = \mathbb{I}_s(x) \times m_s + \big(1 - \mathbb{I}_s(x)\big) \times m_{bg}\ , \qquad (1)$$

where $\mathbb{I}_s(x)$ is the indicator function with value 1 if $x \in \Omega_s$ and 0 otherwise, and m_s, m_{bg} are the material property within and outside of the shape, respectively. The geometry of the shape is characterized by its boundary $\partial\Omega_s$. For inverse problems involving shapes, the goal can then be to minimize a cost functional over the boundary $\partial\Omega_s$ i.e.

$$\min_{\partial\Omega_s} \sum_i \|\mathcal{D}_i f(\boldsymbol{m}) - \boldsymbol{d}_i\|^2, \qquad (2)$$

where $\boldsymbol{m} = [m(x_1),\ m(x_2), \cdots, m(x_n)]$ is the n-dimensional vector of material property at n grid points, $\boldsymbol{d}_i$ are the field measurements at i^{th} location, $f(\cdot)$ is the forward operator and $\mathcal{D}_i$ the projection operator that maps the forward model to the data space..

The *level set* approach introduced by Osher *et al.* (1988) is an elegant way to characterize the evolution of $\partial\Omega_s$, by embedding it in one higher dimensional space via a level set function, $\phi(x)$, such that

$$\begin{cases} \phi(x) > c, \forall\ x \in \Omega_s \\ \phi(x) = c, \forall\ x \in \partial\Omega_s, \\ \phi(x) < c, \forall\ x \in \Omega_{bg.} \end{cases} \qquad (3)$$

In other words, the boundary $\partial\Omega_s$ is defined as a c-level set of the function $\phi(x)$, which allows equation 1 to be re-written as,

$$m(x) = h\big(\phi(x)\big) \times m_s + \Big(1 - h\big(\phi(x)\big)\Big) \times m_{bg}, \qquad (4)$$

where $h(\cdot)$ denotes one of many smooth approximators of the Heaviside step function, such as the *logistic* function in equation 5. The parameter c defines the level-set value and k controls the smoothness of the boundary.

$$h(\,\cdot\,; c, k) = \frac{1}{1+\exp\big(-k(\,\cdot - \boldsymbol{c})\big)} \qquad (5)$$

The main advantage of representing $\partial\Omega_s$ as the c-level set of the function $\phi(x)$ is that its evolution, during an iterative optimization scheme, can be characterized by imposing a Hamilton-Jacobi type of dynamics on $\phi(x)$ (Osher, 1988). The first well-known use of this concept for ill-posed inverse problems can be traced back to the work by Santosa (1996), where the gradient of misfit functional was used to drive the Hamilton-Jacobi dynamics of $\phi(x)$. Because of this tractable approach to evolve the motion of shapes, the level-set method has been used extensively for topology optimization problems (Dijk, 2013). One notable drawback, however, is the computational cost of the level-set method, which scales with the grid size used for domain discretization. Aghasi *et al.* (2011) proposed the *parametric*

10.1190/segam2019-3216897.1

level set (PaLS) method to address this issue, wherein in the level set function $\phi(x)$ is explicitly parameterized as linear expansion of a finite set of basis functions. With a smaller number of basis functions, than the number of grid points, the PaLS method provides a low-dimensional shape representation, which not only can implicitly regularize an ill-posed inverse problem, but also provides opportunities for computational speedup.

We extend the PaLS method for shape-based inversion by first noting its connection with the *Gaussian random fields*. With this viewpoint, one can derive alternate basis that are much more suited, than the PaLS basis, for shape reconstruction and provides further opportunities for dimension reduction. We start the next section with some necessary details on PaLS method followed by an exposition of our method. In the end, we include numerical results from a synthetic subsalt inversion example as a proof of concept.

Theory

The central idea behind PaLS method is to write the level set function as the linear expansion of q local basis functions, i.e.

$$\phi(x) = \sum_{j=1}^{q} \alpha_j \, \psi_j(x; \chi_j), \; \forall x \in \Omega \tag{6}$$

The basis functions ψ_j are local in the sense that their influence is localized to a region in Ω, the extent of which is governed by the parameters χ_j. For instance, a radially symmetric basis function centered at χ_j can be defined as $\psi_j(x; \chi_j) = \psi_j\left(\|x - \chi_j\|_2\right)$. The level set function in equation 6 is, thus, completely characterized by the parameters α_j and χ_j, which allows the minimization problem in equation 2 to be recast as

$$\min_{\alpha_j, \chi_j} \sum_i \|\mathcal{D}_i f(\boldsymbol{m}) - \boldsymbol{d}_i\|^2. \tag{7}$$

Note that the dependence of the cost function on the parameters α_j, χ_j is implicit through the material property vector $\boldsymbol{m}$. Recently, Kadu *et al.* (2016, 2017) used this approach for salt inversion in an FWI framework. Their main idea was to affix the basis function ψ_j on a grid coarser than the grid used for forward modeling and seek a minimizer of equation 7 only over the coefficients α_j. A coarser grid reduces computational complexity, but at the cost of reduced salt reconstruction capability.

We argue that the aforementioned trade-off between the number of basis functions and the reconstruction accuracy can be completely circumvented. A set of alternate basis functions can be derived that span the same function space as a large -possibly infinite- number of canonical basis in equation 6. More importantly, the alternate basis can be restricted to a finite set as they are ordered in terms of their ability to approximate the function space The key insight is that for a certain class (positive definite) of canonical basis, the level-set function $\phi(x)$ can be viewed as a *Gaussian random field* (GRF) defined over the domain Ω (Fasshauer, 2015, p. 90). In other words, level-set function evaluated on any n points in Ω has a multivariate Gaussian distribution with mean $\boldsymbol{\mu} \in \mathbb{R}^n$ and covariance $K \in \mathbb{R}^{n \times n}$, i.e.

$$\{\phi(x_1), \phi(x_2), \cdots, \phi(x_n)\} \sim \text{MVN}(\boldsymbol{\mu}, K),$$

where the $(i,j)^{th}$ element of K is obtained using the canonical basis i.e. $K_{ij} = \psi_j(x_i; x_j)$. The choice of n points is rather arbitrary and thus can be chosen to be the nodes of the finer grid used for forward modeling. Figure 1 illustrates two examples of GRFs on a square domain, uniformly gridded into 100 x 100 cells. A zero-mean GRF with *squared-exponential* kernel, with the following form, is chosen to generate the illustrated fields.

$$K_{ij} = \psi_j(x_i; x_j) = \exp\left(-\|x_i - x_j\|^2 / \sigma^2\right)$$

The parameter σ controls the smoothness of the GRF. The left column of Figure 1 shows two realizations with $\sigma = 2$ and $\sigma = 5$. Each realization amounts to sampling from a multivariate Gaussian with a known mean (zero vector in this case) and the covariance matrix K. The smoothness of the field increases with the parameter σ. The right column shows the same fields but after a smooth Heaviside transformation via equation 5 with $c = 1$ and $k = 10$.

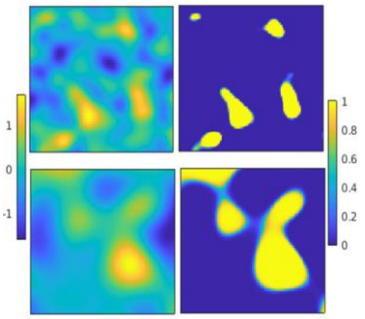

Figure 1: (LEFT column) realizations from zero-mean GRFs with smoothing parameter, $\sigma = 2$ (top) and $\sigma = 5$ (bottom). (RIGHT column) the same fields after a smooth Heaviside transformation to yield shapes of varying geometries.

Given that the level set function $\phi(x)$ is now a GRF, we appeal to the *Karhunen-Loeve* theorem (Fasshauer, 2015, p. 31) to obtain a convenient way to represent it. The theorem states that $\phi(x)$ –a GRF with mean $\boldsymbol{\mu} \in \mathbb{R}^n$ and covariance kernel $K \in \mathbb{R}^{n \times n}$– admits an expansion of the form

$$\phi(x) = \boldsymbol{\mu} + \sum_{j=1}^{n} \alpha_j \sqrt{\lambda_j} \varphi_j(x), \;\; \forall x \in \Omega\,, \tag{8}$$

where λ_j and φ_j are the eigenvalues and the respective orthonormal eigenvectors associated with the symmetric, positive-definite matrix K. The key point is that the summation can be truncated, say up to m terms, based on the positive eigenvalues in order to make the discarded "tail" arbitrarily small. Thus, if $m \ll n$, one can achieve a low dimensional approximation of $\phi(x)$. Note that in the limit of infinitesimally finer gridding, eigenvectors take the form of eigenfunctions and the summation in equation 8 tends to

10.1190/segam2019-3216897.1

DOI:10.1190/segam2019-3216897.1

infinity. In fact, irrespective of the choice of canonical basis ψ_j, the orthonormal basis $\{\varphi_j\}_{j=1}^{\infty}$ so obtained can represent any L_2 function f in the domain Ω as a uniformly convergent series (Fasshauer, 2015, p. 31) i.e.

$$\lim_{n\to\infty}\left(\sum_{j=1}^{n}\langle f,\varphi_j\rangle_{L_2(\Omega)}\times\varphi_j(x)\right)=f(x),\forall\, x\in\Omega \qquad (9)$$

where $\langle\cdot,\cdot\rangle_{L_2(\Omega)}$ denotes the L_2-inner product of two real valued functions in domain Ω.

An important implication of the suggested truncation in equation 8 is that the number of retained eigenvectors is independent of the grid size for a given canonical basis. This is of a great practical advantage because it completely obviates the need to define a coarser grid as in the work by Kadu *et al.* (2017) in order to keep the computations tractable. Additionally, the orthonormal basis φ_j, unlike the canonical basis ψ_j, are global and allows much better shape reconstruction with the same sized basis-set. To demonstrate that we show the shape reconstruction performance using the two types of basis on a 200x200 square domain. Shapes of varying geometries are chosen as shown in figure 2, first row. The shape reconstruction can then be cast as an optimization problem i.e.

$$\min_{\alpha_j}\left\|h\left(\sum_{j=1}^{m}\alpha_j\xi_j\,;1{,}10\right)-y_{true}\right\|_2^2, \qquad (10)$$

where, $y_{true}\in\mathbb{R}^{40000\times1}$ is the binary vector with the true shape, $h(\cdot\,;c,k)$ is the Heaviside approximation as in equation 5 with $c=1$ and $k=10$, and ξ_j is the j^{th} basis vector, canonical (ψ_j) or orthonormal (φ_j). The canonical basis are chosen to be the squared-exponential kernels with $\sigma=2$, centered on coarser 14x14 grid that is placed uniformly over the finer 200x200 grid. This yields 14^2 =196 basis vectors of length 200^2 =40000. The alternate basis vectors are obtained by performing the aforementioned procedure involving eigendecomposition of the symmetric positive-definite matrix $K\in\mathbb{R}^{40000\times40000}$, constructed on the finer grid using the same squared-exponential kernel. The eigenvectors corresponding to the 196 leading eigenvalues are retained for shape reconstruction. Since the objective function in equation 10 is smooth with respect to α_js, the minimization can be carried out using a variety of derivative based algorithms. We used L-BFGS algorithm with Wolfe line search for this purpose. The results are plotted in figure 2, which clearly shows improved shape reconstruction using the orthonormal basis. The last row shows the performance of the L-BFGS algorithms where the misfit function at an arbitrary iteration is plotted against the number of function and gradient evaluations incurred so far. The faster convergence of the algorithm with orthonormal basis is evident, which suggests that the resulting optimization problem is better posed. Fast convergence is a highly desirable feature for large PDE-based models, where the forward and the gradient evaluations can be extremely expensive.

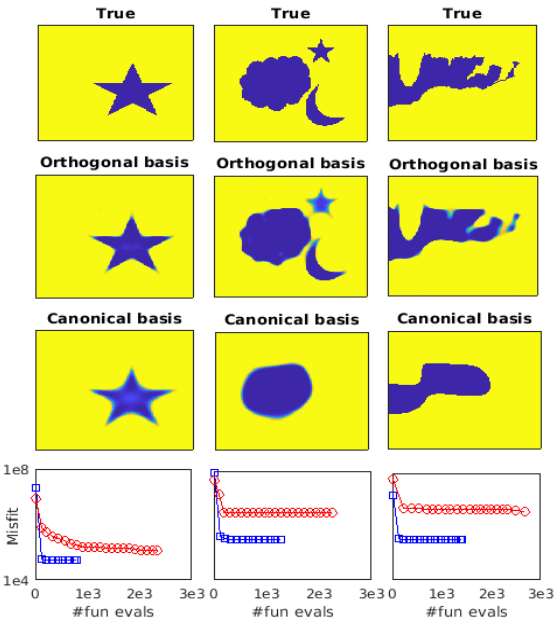

Figure 2: Three example (along each column) of shape resconstruction using the canonical and othonormal basis vectors. The left two examples are shapes of varying complexities. The rightmost shape corresponds to the geometry of BP salt model. The last row plots the evolution of shape misfit (red- canonical, blue- orthonormal) during the optimization procedure and is plotted against the number of forward model evaluation.

A quick note on the eigendecomposition of matrix $K\in\mathbb{R}^{n\times n}$ when n is very large (3-D domains and/or finer grids). This matrix can be prohibitively large to store let alone factorize. In such scenarios, the choice of canonical basis plays a critical role. A compactly supported canonical basis function, such as the *Wendland* kernel used by Aghasi *et al.* (2011), induces sparsity in the matrix K, thereby making it amenable to factorization methods that exploit sparsity (Paige, 1971). Alternatively, once can leverage matrix-free factorization methods (Cullum, 2012; Halko, 2011), which only require the ability to compute the action of K on an arbitrary vector.

Example of salt inversion in FWI framework

We demonstrate the applicability of the proposed method for salt inversion using a synthetic subsurface model inspired by the SEG Advanced Modelling (SEAM) dataset, though made smaller and restricted to two-dimensions. The true subsurface with a salt body is shown in figure 3 (left). A smooth version of the domain without the salt is shown in figure 3 (right). The model represents an 8km x 8km domain,

10.1190/segam2019-3216897.1

DOI:10.1190/segam2019-3216897.1

uniformly discretized in a 400x400 grid resulting in $\boldsymbol{n} = \mathbf{160,000}$ cells. The sources (100) and receivers (300) are positioned uniformly at the top. A 5Hz, Ricker wavelet is used to excite the domain at each source location. The data is recorded for 9 seconds by each receiver. The resulting optimization problem is the same as in equation 2 with $\boldsymbol{m}$, $\boldsymbol{d_i}$ and $\boldsymbol{f}(\cdot)$ being the unknown parameter (Vp) vector, the recorded waveform at the i^{th} receiver, and the acoustic forward operator, respectively. For computational speedup, the forward operator propagates all sources simultaneously with a random source encoding scheme as proposed by Krebs *et al.* (2009). The vector $\boldsymbol{m}$, in the shape-based representation, can be expressed as a convex combination of the salt Vp (4400 m/s) and the known background Vp (figure 3, left). The unknown boundary of the shape is characterized by a level set function, which in turn is specified using a set of 130 orthonormal basis vectors, following the exposition of our method. After a few straightforward algebraic manipulation the objective function can be written as

$$\min_{\boldsymbol{\theta}} \sum_i \left\| f\left(h(B\boldsymbol{\theta}; c, k) \times m_s + \left(1 - h(B\boldsymbol{\theta})\right) \times m_{bg}\right) - d_i \right\|^2 \quad (11)$$

where $h(\cdot\,; c, k)$ is given in equation 5 with $c = 1$ and $k = 10$, and $B \in \mathbb{R}^{40000\times 130}$ is a matrix comprising of orthonormal vectors. The gradient and the Jacobian of the objective function with respect $\boldsymbol{\theta}$ can obtained with the chain rule. We employ Gauss-Newton algorithm to minimize equation 11 with initial value of $\boldsymbol{\theta} = 0$, which makes the

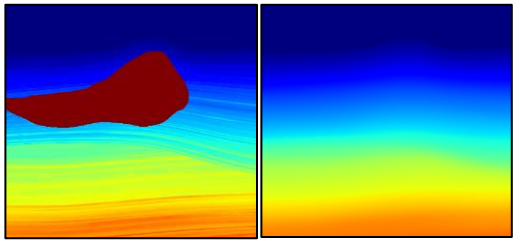

Figure 3: (LEFT) a 2-d subsurface model which serves as the ground truth for our analysis. (RIGHT) a smooth approximation of the background, which is assumed to be known.

starting subsurface model same as the smooth background shown in figure 3 (right). Figure 4 (left) shows the inverted subsurface after 500 iterations using the proposed method. Note that the background was fixed during this process, and the goal was to only invert for the salt body. Figure 4 (right) shows the subsurface after 1000 iterations of traditional cell-based FWI with Tikhonov regularization. As expected, most of the salt geometry –except for the top- couldn't be recovered. Furthermore, figure 5 (left) shows the subsurface model after an additional 500 iteration of cell-based FWI, but now initialized with the recovered salt body. The improved performance of cell-based FWI, when seeded with the right salt geometry, is clearly evident if we compare figure 5 (left) with the ground truth in figure 3 (left). Figure 5 (right) plots the misfit vs. the iteration for this two staged inversion employed in the current example. After recovering

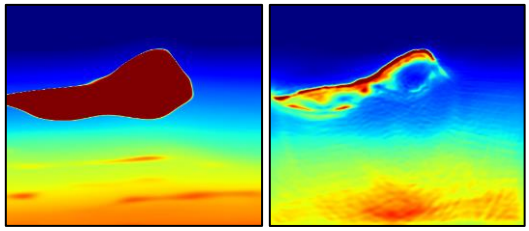

Figure 4: (LEFT) The recovered subsurface after 500 iteration of the low-dimensional, shape-based FWI. The salt body seems to reconstructed in its entirety when compared with the ground truth in figure 2 (left). (RIGHT) The recovered subsurface after 1000 iterations of the traditional cell-based FWI. Note that the majority of the salt body could not be recovered except for the top.

the salt via the proposed shaped-based inversion, the misfit drops another order of magnitude. This observation is due to the fact that the cell-based FWI, now equipped with correct salt geometry, can resolve the subsalt reflectors much more effectively.

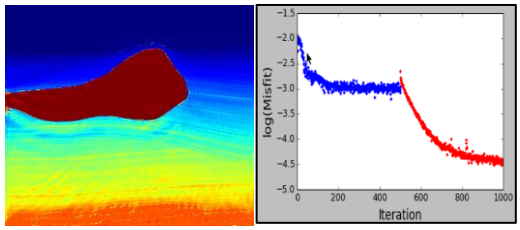

Figure 5: (LEFT) The recovered subsurface after an additional 500 iteration of the cell-based FWI, but now initialized with the subsurface in figure 4 (left). (RIGHT) FWI misfit vs. the number of iteration. The first 500 iterations in blue target only the salt inversion using the proposed method, given a smooth background model. The next 500 iterations in red perfrom cell-based FWI on the entire domain, but using the subsurface model from 500th iteration as the initial model.

Conclusion

We propose an attractive, low dimensional representation of homogeneous geobodies and demonstrate its applicability for salt inversion in an FWI framework. Our approach extends the idea of parametric level-set (PaLS) method, which was proposed as a more tractable alternative to the traditional level-set methods for ill-posed inverse problems involving shapes. Our method improves upon the PaLS parameterization by providing opportunities for further dimension reduction, while retaining the ability to represent myriad of complex salt geometries. We demonstrate, using a synthetic example, that such low dimensional representation improves our ability to invert for salt, in addition to providing avenues for computational speedup.

10.1190/segam2019-3216897.1

REFERENCES

Aghasi, A., M. Kilmer, and E. L. Miller, 2011, Parametric level set methods for inverse problems: SIAM Journal on Imaging Sciences, **4**, 618–650, doi: https://doi.org/10.1137/100800208.

Cullum, J. K., and R. A. Willoughby, 2012, Lanczos algorithms for large symmetric eigenvalue computations: Progress in scientific computing, **vol. 3**: Birkhäuser.

Fasshauer, G. and M. McCourt, 2015*a*, 2.2: Hilbert-Schmidt, Mercer and Karhunen-Loeve series: Kernel-based approximation methods using MATLAB: Interdisciplinary mathematical sciences, **vol. 19**: World Scientific, 17–39.

Fasshauer, G. and M. McCourt, 2015*b*, 5.1: Random Fields and random variables: Kernel-based approximation methods using MATLAB: Interdisciplinary Mathematical Sciences, **vol. 19**: World Scientific, 90–95.

Guo, Z., and M. V. de Hoop, 2013, Shape optimization and level-set method in full waveform inversion with 3D body construction: 83rd Annual International Meeting, SEG, Expanded Abstracts, 1079–1083, doi: https://doi.org/10.1190/segam2013-1057.1.

Halko, N., P.-G. Martinsson, and J. A. Tropp, 2011, Finding structure with randomness: stochastic algorithms for constructing approximate matrix decompositions: SIAM Review, **53**, 217–288, doi: https://doi.org/10.1137/090771806.

Kadu, A., T. Van Leeuwen, and W. A. Mulder, 2016, A parametric level-set approach for seismic full-waveform inversion: 86th Annual International Meeting, SEG, Expanded Abstracts, 1146–1150, doi: https://doi.org/10.1190/segam2016-13870276.1.

Kadu, A., T. van Leeuwen, and W. A. Mulder, 2017, Salt reconstruction in full-waveform inversion with a parametric level-set method: IEEE Transactions on Computational Imaging, **3**, 305–315, doi: https://doi.org/10.1109/TCI.2016.2640761.

Kalita, M., V. Kazei, Y. Choi, and T. Alkhalifah, 2018, Regularized full waveform inversion for salt-bodies: 88th Annual International Meeting, SEG, Expanded Abstracts, 1043–1047, doi: https://doi.org/10.1190/segam2018-2995963.1.

Krebs, J. R., J. E. Anderson, D. Hinkley, R. Neelamani, S. Lee, A. Baumstein, and M. D. Lacasse, 2009, Fast full-wavefield seismic inversion using encoded sources: Geophysics, **74**, no. 6, WCC177–WCC188, doi: https://doi.org/10.1190/1.3230502.

Lewis, W., B. Starr, and D. Vigh, 2012, A level-set approach to salt geometry inversion in full waveform inversion: 82nd Annual International Meeting, SEG, Expanded Abstracts, 1–5, doi: https://doi.org/10.1190/segam2012-0737.1.

Maranganti, R., and Y. Agnihotri, 2014, Hybrid target-oriented salt interpretation in the Gulf of Mexico: Interpretation, **2**, no. 4, SL21–SL28, doi: https://doi.org/10.1190/INT-2014-0038.1.

Mosher, C., E. Keskula, J. Malloy, R. Keys, H. Zhang, and S. Jin, 2007, Iterative imaging for subsalt interpretation and model building: The Leading Edge, **26**, 1424–1428, doi: https://doi.org/10.1190/1.2805763.

O'Briain, M., D. Smith, C. Montoya, B. Burgess, S. Koza, O. Zdraveva, M. Ishak, S. Alwon, R. King, D. Nikolenko, and S. Vautier, 2013, Improved subsalt imaging and salt interpretation by RTM scenario testing and image partitioning: 83rd Annual International Meeting, SEG, Expanded Abstracts, 3856–3860, doi: https://doi.org/10.1190/segam2013-0742.1.

Osher, S., and J. A. Sethian, 1988, Fronts propagating with curvature-dependent speed: Algorithms based on Hamilton-Jacobi formulations: Journal of Computational Physics, **79**, 12–49, doi: https://doi.org/10.1016/0021-9991(88)90002-2.

Paige, C. C., 1971, The computation of eigenvalues and eigenvectors of very large sparse matrices: Ph.D. Thesis: The University of London.

Santosa, F., 1996, A level-set approach for inverse problems involving obstacles: ESAIM-Control, Optimisation and Calculus of Variation, **1**, 17–33, doi: https://doi.org/10.1051/cocv:1996101.

van Dijk, N. P., K. Maute, M. Langelaar, and F. van Keulen, 2013, Level-set methods for structural topology optimization: A review: Structural and Multidisciplinary Optimization, **48**, 437–472, doi: https://doi.org/10.1007/s00158-013-0912-y.